

Learning Bayes-optimal dendritic opinion pooling

Jakob Jordan^{1*}, João Sacramento^{1,3}, Willem A.M. Wybo^{1,4},
Mihai A. Petrovici^{1,2†} & Walter Senn^{1†}

¹Department of Physiology, University of Bern, Bern, Switzerland

²Kirchhoff-Institute for Physics, Heidelberg University, Heidelberg, Germany

³Institute of Neuroinformatics, UZH / ETH Zurich, Zurich, Switzerland

⁴Institute of Neuroscience and Medicine, Forschungszentrum Jülich, Jülich, Germany

April 28, 2021

Abstract

Pooling different opinions and weighting them according to their reliability is conducive to making good decisions. We demonstrate that single cortical neurons, through the biophysics of conductance-based coupling, perform such complex probabilistic computations via their natural dynamics. While the effective computation can be described as a feedforward process, the implementation critically relies on the bidirectional current flow along the dendritic tree. We suggest that dendritic membrane potentials and conductances encode opinions and their associated reliabilities, on which the soma acts as a decision maker. Furthermore, we derive gradient-based plasticity rules, allowing neurons to learn to represent desired target distributions and to weight afferents according to their reliability. Our theory shows how neurons perform Bayes-optimal cue integration. It also explains various experimental findings, both on the system and on the single-cell level, and makes new, testable predictions for intracortical neuron and synapse dynamics.

Introduction

Successful decision making is based on well-considered arguments. This holds as true for individuals as it does for whole societies. For instance, opinions on proposed legislature may vary between experts, political parties and special interest groups. How should one combine these different opinions? One might, for example, integrate the different opinions by weighting them according to their relative reliability, estimated from their past performance, or demonstrated expertise. The final decision can then be based on the joint, reliability-weighted opinion, representing a compromise.

Such problems of weighting and combining different opinions are commonplace for our brains. Whether inputs from neurons with different receptive fields or inputs from different modalities (Fig. 1a), our cortex needs to combine these uncertain information sources into a coherent whole. Previous work has demonstrated that multiple interacting neuronal populations can efficiently perform such probabilistic

*Correspondence: jakob.jordan@unibe.ch

†Joint senior authorship.

computations [1, 2]. These studies provided mechanistic models for the often Bayes-optimal behavior observed in humans and other animals [3–5]. Here we demonstrate that probabilistic computations are even deeper ingrained in our biological substrate, in single cortical neurons.

In cortical neurons, each dendritic branch receives information from presynaptic partners and forms a local membrane potential. We propose this to be the analog of an opinion. In the absence of other compartments and leak currents, the somatic output, the analog of a decision, would reflect the opinion of the single branch. However, in the presence of the leak and multiple branches, the soma encodes a reliability-weighted combination of a prior and additional opinions. We further propose that the reliability of a dendritic branch with regards to a particular local opinion is encoded in its local conductance, including conductances elicited by synaptic input. The biophysics of the bidirectional current flow in cortical neurons with multiple dendritic compartments naturally implements Bayesian opinion weighting (Fig. 1b), while the output of the neuron encodes decisions based on the pooled opinions.

Formally, the neuronal operation can be described as computing a posterior distribution. The crucial ingredient is the divisive normalization performed by conductance-based synaptic coupling [6]. While the dendritic opinion weighting emerges from the recurrent interaction of multiple compartments within the dendritic tree, at the level of the input-output transfer function, the effective computation can be described in a feed-forward manner.

Beyond opinion weighting itself, the single-neuron view provides an efficient basis for learning these weights. Synapses not only learn to reproduce a somatic target activity [7], but they also adjust synaptic weights to achieve some target variance in the somatic potential. Furthermore, afferents with low reliability will be adjusted to contribute with a smaller total excitatory and inhibitory conductance to allow other projections to gain more influence. Implicitly, this allows each dendritic compartment to adjust its relative reliability according to its past success in contributing to the somatic decision.

In our theoretical framework we derive somatic membrane potential dynamics and synaptic plasticity jointly via stochastic gradient ascent on the log-posterior distribution of somatic potentials. Simulations demonstrate successful learning of a prototypical opinion weighting task, and the integration of sensory cues from different modalities to guide behavior. The trained model allows us to interpret behavioral and neuronal data from cue integration experiments through a computational lens and to make specific predictions about both system behavior and single cell dynamics.

Results

Opinion weighting in cortical neurons

We consider a prototypical example of neuronal opinion weighting: the integration of various cues about a stimulus, for example in early visual areas from different parts of the visual field (Fig. 1a) or in association areas from different sensory modalities (Fig. 1b).

Due to properties of the stimulus and of our sensory systems, information delivered via various modalities inherently differs in reliability. Behavioral evidence demonstrates that humans and non-human animals are able to integrate sensory input from different modalities [e.g., 3–5, 8–13] and prior experience [e.g., 14, 15], to achieve a similar performance as Bayes-optimal cue-integration models. We suggest that pyramidal cells across cortex naturally take the average reliability of their inputs into account using two orthogonal information channels: membrane potentials and conductances.

Consider a situation where your visual sensory apparatus is impaired, for example, due to a deformation of the lens. Presented with multimodal stimuli that provide auditory and visual cues, you would have learned to rely more on auditory cues rather than visual input (Fig. 2). When confronted with an animal as

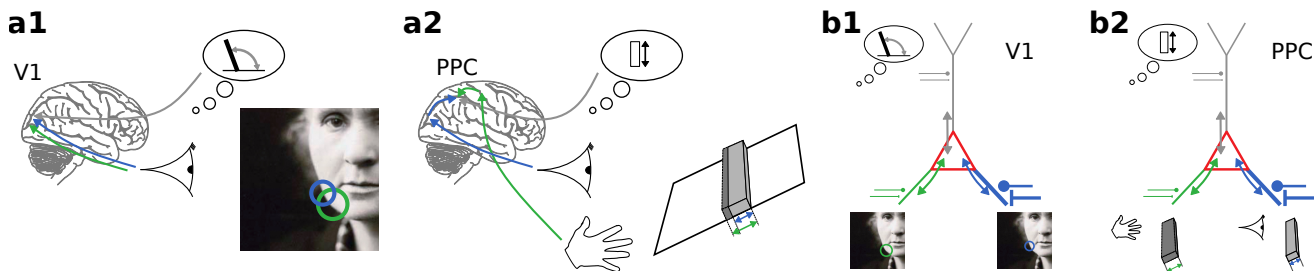


Figure 1: **Dendritic opinion weighting as a canonical neuronal operation across cortex.** **(a1)** Cue integration in early visual perception judging the orientation of a local edge. **(a2)** Cue integration in multimodal perception judging the height of a bar [3]. **(b1)** Dendritic opinion weighting of visual cues combining information across receptive fields. **(b2)** Dendritic opinion weighting of multisensory cues combining information across modalities. This probabilistic computation is realized by the bidirectional voltage propagation in cortical neurons (colored arrows) that settles at the pooled somatic opinion (red triangle). The somatic voltage represents the reliability-weighted dendritic opinions (grey, green, blue), calculated by a biophysical "consensus finding".

in Fig. 2a, based on your vision alone, you might expect it to be a cat, but not be certain about it. Hearing it bark, however, would shift your belief towards it being, with high certainty, a dog. Since current-based neurons only encode opinions about their preferred feature in the total synaptic current without considering the relative reliability of different pathways, they can generate wrong decisions: here, a neuron that integrates auditory and visual cues wrongly signals the presence of a cat to higher cortical areas (Fig. 2b). In contrast, by using dendritic conductances g^d as an additional coding dimension besides effective dendritic reversal potentials E^d , conductance-based neurons are able to respond correctly by weighting auditory inputs stronger than visual inputs (Fig. 2c). In the absence of stimuli, the "cat neuron" has a low prior opinion that a cat may be present, but clearly increases this opinion upon the presentation of an ambiguous cat-dog image (Fig. 2e, 400 – 1200ms, d,e). When the animal subsequently barks, the opinion about the presence of a cat drops, i.e., the somatic membrane potential of the cat neuron hyperpolarizes, while the reliability for this updated opinion increases, i.e., conductances increase. Consistent with Bayes-optimal cue-integration models [e.g., 16], the combined estimate shows an increased reliability, even if the cues are opposing.

The neuronal opinion code

Excitatory and inhibitory conductances targeting a dendritic compartment combine with the dendritic leak and the associated reversal potentials into a total dendritic transmembrane current $I^d = g^d (E^d - u^d)$. Here, the local, stimulus-dependent dendritic reversal potential E^d is given by

$$E^d = \frac{g^E E^E + g^I E^I + g^L E^L}{g^E + g^I + g^L}, \quad (1)$$

where excitatory, inhibitory and leak reversal potential are denoted as $E^{E/I/L}$, and the respective conductances by $g^{E/I/L}$. The sum of these three conductances $g^d = g^E + g^I + g^L$ represents the isolated dendritic conductance, which excludes the somato-dendritic coupling. The excitatory and inhibitory conductances are the product of the synaptic weights times the presynaptic firing rates, $g^{E/I} = W^{E/I} r$. Note that in general E^d is different from the actual dendritic potential u^d , which is additionally influenced by the somatic potential.

In our framework, each dendritic compartment has an associated preferred feature, i.e., an activity pattern in its afferents which maximizes its reversal potential E^d . We hence identify E^d with the dendritic

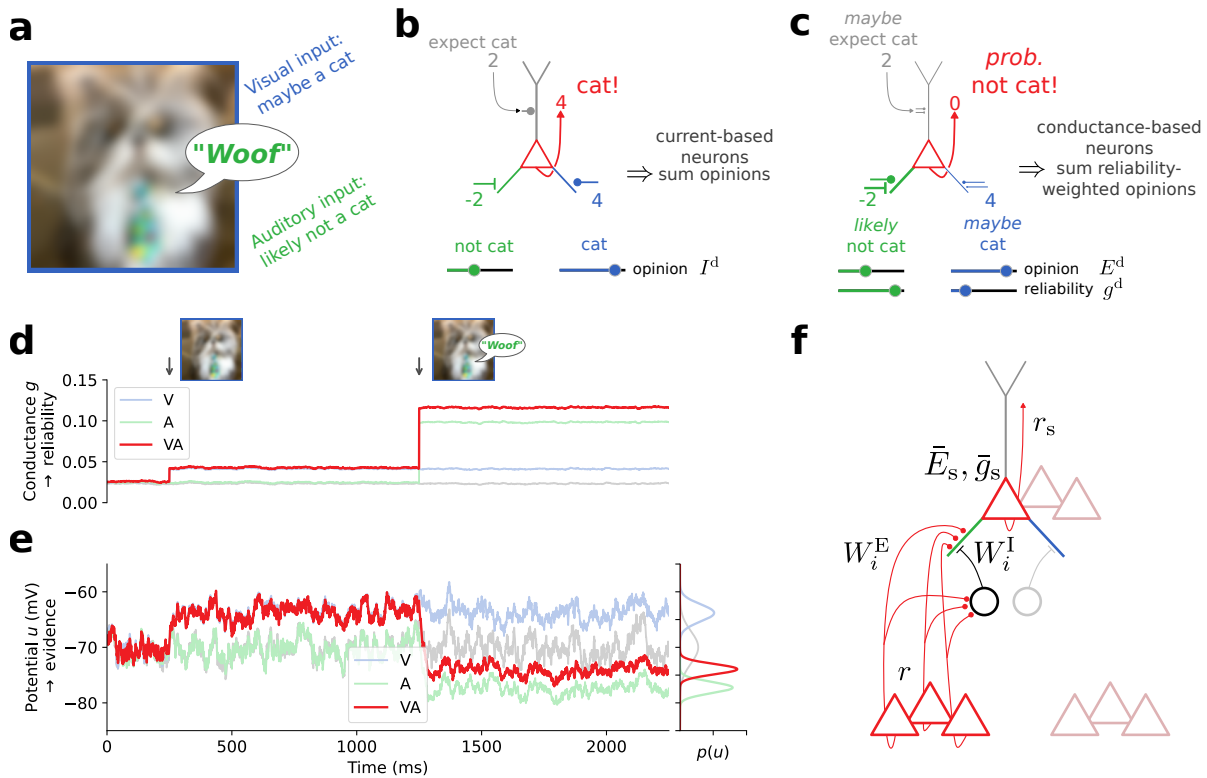


Figure 2: **Conductance-based neuronal dynamics naturally implement probabilistic cue integration.** (a) A multisensory stimulus. (b) Current-based neurons can only additively accumulate opinions about their preferred feature. (c) Conductance-based neurons simultaneously represent opinions and associated reliability. (d) Total somatic conductances \bar{g}_s consisting of leak and synaptic conductances in a multisensory neuron under three conditions: only visual input (V, blue), only auditory input (A, green), bimodal input (VA, red), and no input (gray). Before 400ms the visual cue is absent. Before 1200ms the auditory cue is absent. (e) Somatic membrane potentials u_s are noisy, time-continuous processes that sample from the somatic distributions in the respective condition. This histogram on the right shows the somatic voltage distributions between 1250ms and 2250ms. (f) Suggested microcircuit implementation. Activity r of pyramidal cells from lower areas is projected directly (red lines with circular markers, W_i^E denote excitatory synaptic weights) and indirectly via inhibitory interneurons (circles and black lines with bar markers, W_i^I denote inhibitory synaptic weights) to different dendritic compartments of pyramidal cells in higher cortical areas. Each pyramidal cell represents a pooled opinion \bar{E}_s with some associated inverse variance \bar{g}_s distributed across a corresponding population (overlapping triangle triples, representing pre- and postsynaptic opinions, respectively).

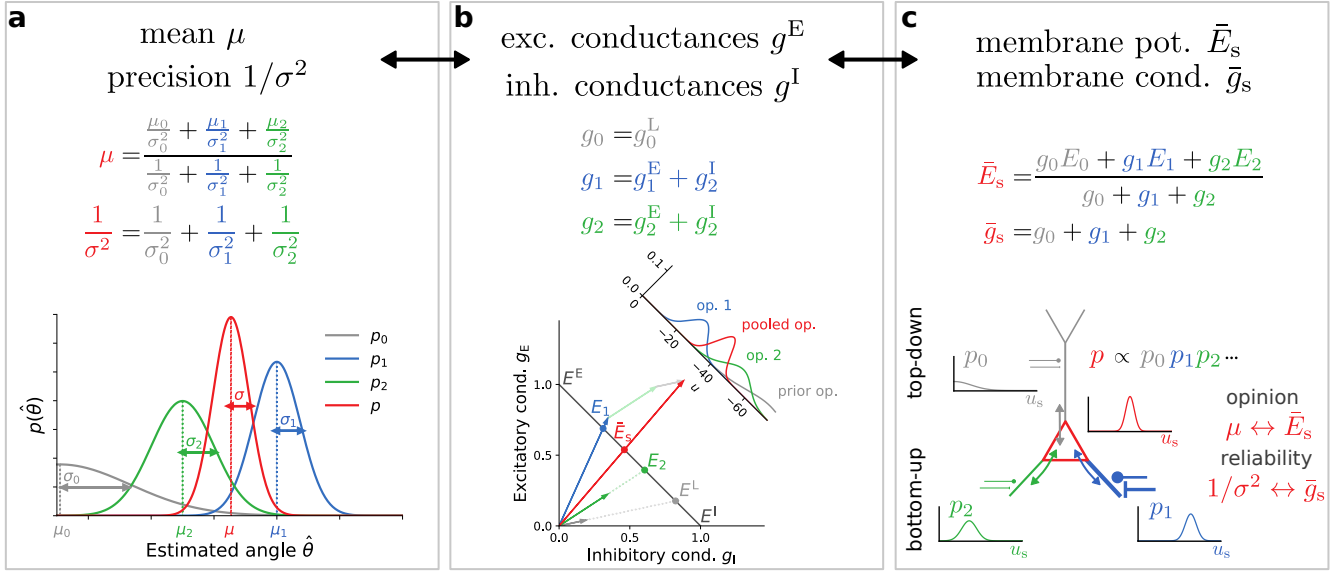


Figure 3: Non-linear opinion weighting is achieved through a linear vector summation of conductances. (a) Non-linear combination of Gaussian probability densities. The pooled mean is a convex combination of the original means, while the pooled reliability, the inverse variance, is a sum of the individual reliabilities. (b) Stimulus-evoked excitatory and inhibitory synaptic conductances as two-dimensional vectors (blue and green), as well as the leak (gray), are linearly summed across dendrites to yield the total somatic conductances (red arrow). The intersections with the antidiagonal (black line) yield the corresponding dendritic and somatic reversal potentials. This intersection is a nonlinear operation (see Methods, "Linear coordinates for nonlinear processing"). The inset shows the full distributions. Note that the prior can in general be modulated by synaptic conductance elicited by top-down input (see panel c). (c) Translation of prior (gray) and dendritic (green and blue) opinions and reliabilities into the corresponding somatic mean voltage and conductances (red). Note that for visualization purposes, the prior distribution is only partially shown.

opinion about how well presynaptic activity is compatible with its preferred feature. We furthermore identify the isolated dendritic conductance g^d with the reliability of the corresponding dendritic opinion. Intuitively speaking, the opinion of a dendritic compartment with large dendritic conductance will be more resilient against different opinions encoded in other compartments.

How are dendritic opinions pooled to jointly determine the output of a neuron? The interaction between soma and dendrites in cortical neurons naturally form a pooled opinion \bar{E}_s as a weighted average of the individual dendritic opinions E_i^d , with the weight of each dendritic opinion reflecting its reliability g_i^d (Fig. 3c). The reliability of this pooled opinion is reflected by the total somatic conductance \bar{g}_s . The somatic membrane potential u_s dynamically traces a noisy estimate of the pooled opinion \bar{E}_s ,

$$C\dot{u}_s = \bar{g}_s (\bar{E}_s - u_s) + \xi$$

$$= g_0(E_0 - u_s) + \sum_{i=1}^D \alpha_i^{\text{sd}} [g_i^L(E^L - u_s) + g_i^E(E^E - u_s) + g_i^I(E^I - u_s)] + \xi, \quad (2)$$

with membrane capacitance C , and dendro-somatic coupling factors $\alpha_i^{\text{sd}} = g_i^{\text{sd}} / (g_i^{\text{sd}} + g_i^d)$ that result from the dendro-somatic coupling conductances g_i^{sd} and the isolated dendritic conductances g_i^d (see Methods, "Bayesian theory of somatic potential dynamics" for details).

The corresponding neuronal processing of inputs is a non-linear operation on the level of membrane potentials, described by sublinear summations [17]. Despite the nonlinear effect of inputs on membrane potentials, the operations in conductance space are described by purely linear operations. While the

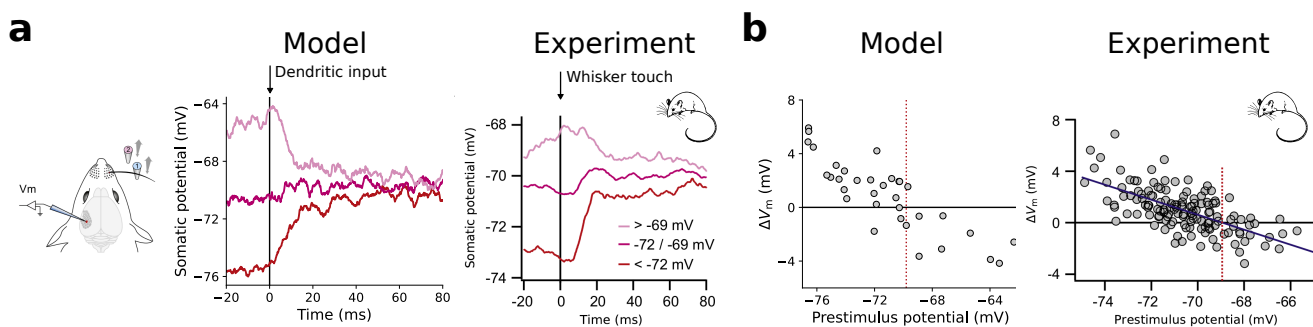


Figure 4: **Dendritic opinion pooling implies stimulus-specific reversal potentials.** (a) Average stimulus-evoked responses for different ranges of prestimulus potentials generated by our model (left) and measured experimentally (right, from [18]). Vertical arrow indicates stimulus onset corresponding to activation of dendritic input and whisker touch, respectively. (b) PSP amplitude vs. prestimulus potential generated by our model (left) and measured experimentally (right, from [18]). Reprinted from *Neuron*, 69, Crochet, S., Poulet, J. F., Kremer, Y. & Petersen, C. C., Synaptic mechanisms underlying sparse coding of active touch, 1160–1175., Copyright (2011), with permission from Elsevier.

dendritic sublinearity gives rise to dendritic opinions, the somatic sublinearity performs a Bayesian combination of opinions across the dendritic tree (Fig. 3a,c).

The somatic membrane potential is transformed into an instantaneous output rate $r_s = \rho(u_s)$ via some monotonically increasing transfer function ρ . At any given time, multiple neurons with identical preferred features will produce different output rates due to random background input. The variance across such an ensemble reflects the reliability of the somatic opinions and can thus be communicated to downstream areas (Fig. 2f) which can adjust synaptic weights to take this variability into account.

Stimuli elicit neuron-specific opinions and increase the neuronal reliability

The conductance-centered neuronal opinion weighting framework predicts neuronal response properties that differ from those of classical current-based neuron models. In the opinion weighting framework, prior opinions are encoded in the somatic membrane potential in the absence of sensory input. These priors typically have low reliability, encoded in relatively small conductances. As a consequence the neuron is more susceptible to background noise, resulting in large membrane potential fluctuations around the prior potential. When a cue is presented, presynaptic activity increases, thereby pulling postsynaptic membrane potentials towards the cue-specific reversal potentials E^d , irrespective of their prior value (Fig. 4a). This phenomenon is observed in electrophysiological recordings from mouse somatosensory cortex: the change in membrane potential upon whisker stimulation pulls the somatic membrane potential from variable spontaneous pre-stimulus potentials towards a cue-specific post-stimulus potential (Fig. 4a, [18]). Besides a change in the average membrane potential, cue onset increases conductances and hence decreases spontaneous fluctuations.

These effects are signatures of neuronal opinion weighting. Cues provide information about the presence or absence of a neuron’s preferred feature. Upon cue onset, the prior distribution (i.e., distribution in the absence of cues) is combined with cue-specific distributions leading to an updated somatic distribution with adapted mean and reduced variance. If the prior strongly disagrees with cue information, the change in mean is larger than if prior and cue information are consistent. Importantly, the variance is always reduced in the presence of new information, regardless of whether it conflicts with previous information or not; this is a hallmark of Bayesian reasoning.

We propose that this probabilistic computation underlies the observed stimulus-driven reduction of variability throughout cortex [19, 20] and explains why stimulus-evoked PSP amplitudes are negatively correlated with prestimulus potentials [Fig. 4b; also see 18, 21]. In whisker stimulation experiments [18], the stimulation intensity is encoded by the whisker deflection angle. Our framework predicts that, as the amplitude of whisker deflections increases, the variance of the post-stimulus potentials decreases. This prediction is consistent with the recent observation that increasing the contrast of oriented bar stimuli reduces the variance in the postsynaptic response of orientation-specific neurons in macaque visual cortex [22]. Furthermore, our model predicts that the nature of stimuli during learning will affect the impact of sensory cues on electrophysiological quantities and behavior: more reliable priors will cause a smaller influence of sensory inputs, while increasing stimulus reliability would achieve the opposite effect. Regardless of training, our model also predicts decreasing influence of the prior for increasing stimulus intensity.

Bayesian neuronal dynamics

The proposed neuronal opinion weighting can be described in a probabilistic framework of neuronal coding. This framework allows us to derive the same biophysical dynamics, but from a normative standpoint.

For given synaptic weights W and presynaptic rates r that encode information about sensory stimuli, we propose that the soma computes a posterior distribution over its membrane potential $p(u_s|W, r)$. Absent any sensory input, we assume the somatic voltage follows a Gaussian prior $p(u_s|E_0, g_0)$. Its mean represents the prior somatic opinion E_0 and its variance is the inverse of the prior reliability g_0 (cf. Fig. 3); these parameters are determined by a combination of leak and non-sensory (top-down or lateral) inputs. Consistent with experimental data [23] we assume Gaussian dendritic likelihoods $p(E_i^d|u_s, g_i^d)$ with dendritic reversal potentials E_i^d and isolated dendritic conductances g_i^d determined by synaptic weights and presynaptic rates as discussed above. The dendritic likelihoods quantify the statistical relationship between dendritic opinions and the somatic potential. Intuitively speaking, they describe how compatible a certain somatic potential u_s is with a dendritic reversal potential E_i^d . Note that this relation is of purely statistical, not causal nature – biophysically, dendritic reversal potentials E_i^d cause somatic potentials, not the other way around. To perform probabilistic inference, the soma computes the posterior via Bayes’ theorem:

$$p(u_s|W, r) \propto \text{likelihood} \times \text{prior} = e^{-\frac{\bar{g}_s}{2\lambda_e}(u_s - \bar{E}_s)^2}. \quad (3)$$

Here, \bar{g}_s represents the total somatic conductance, and \bar{E}_s the pooled somatic opinion, which is given by the convex combination of the somatic and dendritic opinions, weighted by their respective reliabilities and dendro-somatic coupling factors (see Methods, ”Bayesian theory of somatic potential dynamics” and Fig. 3). The exploration parameter λ_e relates conductances to membrane potential fluctuations. In general, this parameter depends on neuronal properties, for example, on the amplitude of background inputs and the spatial structure of the cell.

To obtain the somatic membrane potential dynamics from its statistics, we postulate that the soma performs noisy gradient ascent on the log-posterior of the somatic potential:

$$C\dot{u}_s = \lambda_e \frac{\partial}{\partial u_s} \log p(u_s|W, r) + \xi = \bar{g}_s (\bar{E}_s - u_s) + \xi. \quad (4)$$

The additive noise ξ represents white noise with variance $2C\lambda_e$, arising, for example, from unspecific background inputs [24, 25]. For fixed presynaptic activity r , the average somatic membrane potential hence represents a maximum-a-posteriori estimate (MAP, [16]), while its variance is inversely proportional

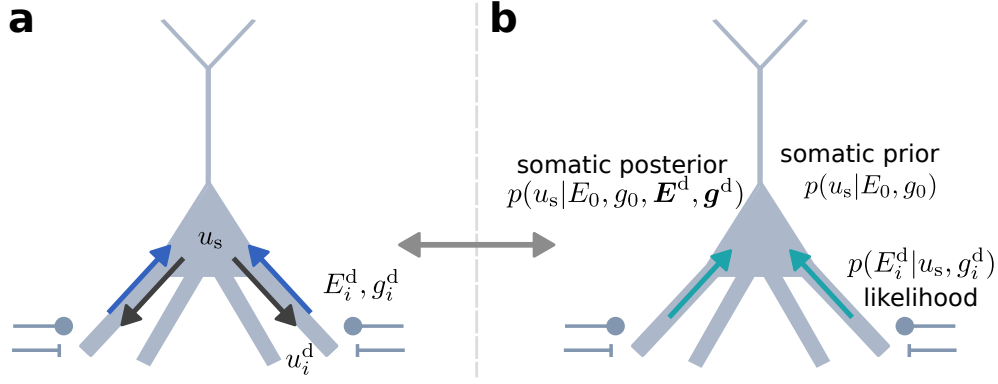


Figure 5: **Single neuron dynamics as Bayesian inference.** (a) Biophysical dynamics bidirectionally couple somatic and dendritic membrane potentials (Eqs. 6, 7). (b) Their steady state can be interpreted as computing the posterior $p(u_s | E_0, g_0, \mathbf{E}^d, \mathbf{g}^d)$ from the somatic prior $p(u_s | E_0, g_0)$ and dendritic likelihoods $p(E_i^d | u_s, g_i^d)$.

to the total somatic conductance \bar{g}_s . The effective time constant of the somatic dynamics is $\tau = C/\bar{g}_s$, thus enabling u_s to converge faster to reliable MAP estimates for larger \bar{g}_s .

The dynamics derived here from Bayesian inference are identical to the somatic membrane potential dynamics in bidirectionally-coupled multi-compartment models with leaky integrator dynamics and conductance-based synaptic coupling under the assumption of fast dendritic responses (Eqn. 2). In other words, the biophysical system effectively computes the posterior distribution via its natural evolution over time. This suggests a fundamental role of conductance-based dynamics for Bayesian neuronal computation, which also extends to synaptic plasticity, as we discuss in the following.

Gradient-based synaptic dynamics

A fixed stimulus determines the somatic membrane potential distribution and – as shown in the previous section – the somatic membrane potential dynamics will continuously sample from this distribution. Prior to learning, this distribution will typically be different from a desired distribution as predicted, for example, by past sensory experience or cross-modal input. We refer to such input-dependent desired distributions as target distributions.

We define learning our framework as adapting synaptic weights W to increase the probability of observing samples u_s^* from the target distribution. Formally, learning reduces the Kullback-Leibler divergence between the target distribution $p^*(u_s | r)$ and the somatic distribution $p(u_s | W, r)$. This is achieved through gradient ascent on the (log-)posterior somatic probability of target potentials u_s^* sampled from the target distribution, resulting in the following dynamics for excitatory and inhibitory weights:

$$\dot{W}_i^{EI} \propto \lambda_e \frac{\partial}{\partial W_i^E} \log p(u_s^* | W, r) \propto \left[\underbrace{(u_s^* - \bar{E}_s) (E^{EI} - \tilde{E}_i^d)}_{=\Delta\mu_i^{EI}} + \underbrace{\frac{\alpha_i^{\text{sd}}}{2} \left(\frac{\lambda_e}{\bar{g}_s} - (u_s^* - \bar{E}_s)^2 \right)}_{=\Delta\sigma^2} \right] r, \quad (5)$$

with $\tilde{E}_i^d = \alpha_i^{\text{sd}} \bar{E}_s + (1 - \alpha_i^{\text{sd}}) E_i^d$, where α_i^{sd} describes an effective coupling strength (see Methods, "Weight dynamics" for details).

All dynamic quantities arising in the synaptic plasticity rule are neuron-local. The dendritic potentials E_i^d are available at the synaptic site, as well as the presynaptic rates r . We hypothesize that the backpropagating action potential rate that codes for u_s^* can influence dendritic synapses [26]. Furthermore, the total conductance \bar{g}_s determines the effective time constant by which the somatic membrane potential fluctuates

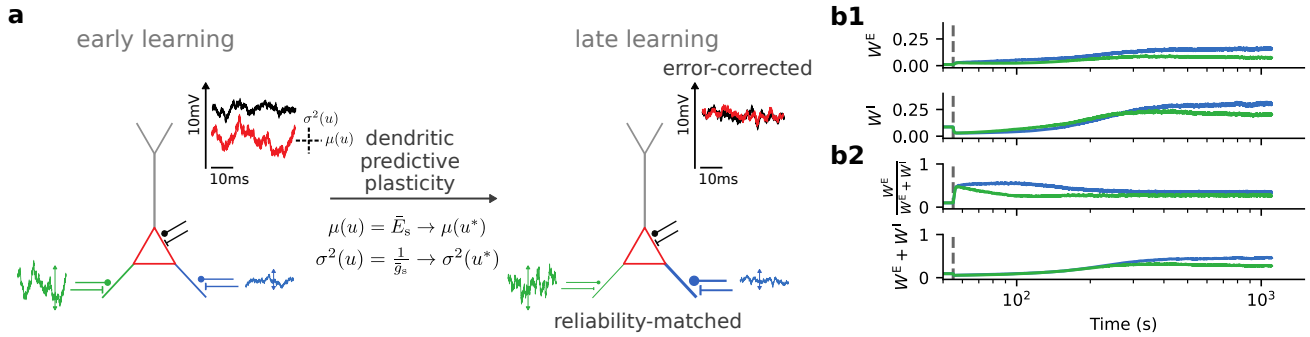


Figure 6: **Dendritic predictive plasticity performs error correction and reliability matching.** (a) A neuron receives input via two different input channels with different noise amplitudes (green and blue). Synaptic plasticity adapts the mean (μ) and variance (σ^2) of the somatic membrane potential (red) towards the target (black). (b1) Excitatory and inhibitory weights per input channel. Dashed vertical line indicates onset of learning. (b2) Top: ratio of excitatory and total synaptic weights. Bottom: total synaptic weights.

and could be measured through its temporal correlation length. The exact molecular mechanisms by which these terms are computed in the synapses remain a topic for future research.

Joint learning of somatic mean and variance

The total postsynaptic error is composed of an error in the mean $\Delta\mu_i^{E/I}$ and an error in the variance $\Delta\sigma^2$ (Eqn. 5). By these two mechanisms, the adaptation of the excitatory and inhibitory synapses jointly reduces both errors, the error in the mean and the error in the variance. To simultaneously adjust both the mean and variance freely, the two degrees of freedom offered by separate excitation and inhibition are required.

To illustrate these learning principles we consider a toy example in which a neuron receives input via two different input channels with different noise amplitudes. Initially neither the average somatic membrane potential, nor its variance match the target distribution (Fig. 6a, left). Over the course of learning, the ratio of excitatory to inhibitory weights increases to allow the somatic membrane potential to match the average target potential and the total strength of both excitatory and inhibitory inputs increases to match the variance of the target (Fig. 6a, right; b1). Excitatory and inhibitory weights hence first move into opposite directions to match the average, and later move in identical directions to match the variance (Fig. 6b1). While the relative strength of excitation and inhibition after learning is comparable for both input channels (Fig. 6b2, top), the total synaptic strength of the less noisy input channel is significantly larger (Fig. 6b2, bottom), reflecting its larger reliability in producing the desired somatic potentials. Intuitively speaking, our plasticity rule adjusts the relative weights of all afferents such that those with high correlation to target potentials are stronger than those with weak correlation.

Our plasticity rules for excitatory and inhibitory synapses thus predict that initially excitatory and inhibitory synaptic strengths move in opposite directions to jointly match the average somatic membrane potential to the target potential. Second, after this mismatch has been sufficiently reduced, excitatory and inhibitory strengths covary in order to match the variance of the target distribution.

Learning Bayes-optimal cue combinations

We next consider a multisensory integration task in which a rat has to judge whether the angle of a grating is larger than 45° or not, using whisker touching (T) and visual inspection (V), see Fig. 7a and [13]. In

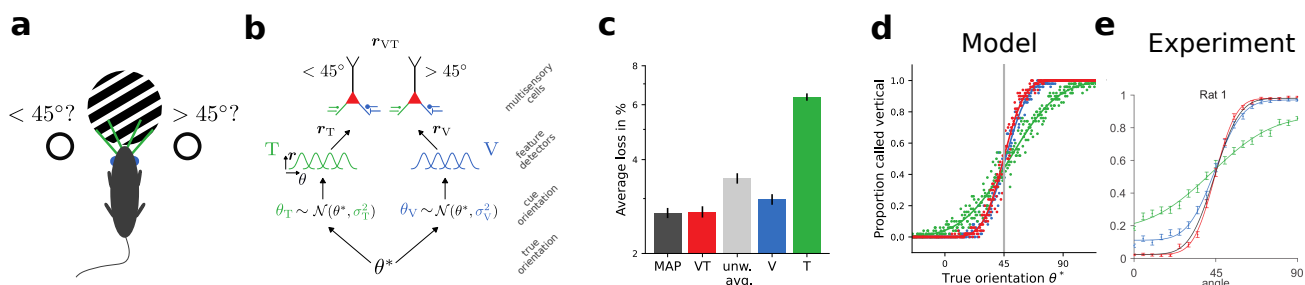


Figure 7: Learning Bayes-optimal inference of orientations from multimodal stimuli. (a) Experimental setup [see also 13]. (b) Network model. (c) Accuracy of the MAP estimate (MAP, dark gray), the trained model with bimodal cues (VT, red), unweighted average of visual and tactile cues (unw. avg., light gray), and the trained model with only visual (V, blue) and tactile cues (T, green), respectively. Error bars denotes standard error of the mean over 25 experiments, each consisting of 20000 trials. (d) Psychometric curves of the model. Dots: subsampled data, solid lines: fit of complementary error function. The inset shows the benefit of bimodal stimulation over unimodal stimulation. The benefit is measured by the difference between the average loss in unimodal (V, T) and the average loss in bimodal (VT) conditions. (e) Psychometric curves for rat 1 [13] for comparison. Reprinted from Neuron, 97, Nikbakht, N., Tafreshiha, A., Zoccolan, D. & Diamond, M. E., Supralinear and supramodal integration of visual and tactile signals in rats: psychophysics and neuronal mechanisms, 626–639, Copyright (2018), with permission from Elsevier.

this example, projections are clustered according to modality on dendritic compartments. In general, this clustering is not necessarily determined by modality but could also reflect, for example, lower-level features, or specific intracortical pathways. In our setup, uncertainty in the sensory input from the two modalities is modeled by different levels of additive noise. The binary classification is performed by two multisensory output neurons that are trained to encode the features $> 45^\circ$ and $< 45^\circ$, respectively. Technically, we assume the target distribution is a narrow Gaussian centered around a stimulus-dependent target potential. For example, for the neuron encoding orientations $> 45^\circ$ and it would be low otherwise. The output neurons receive input from populations of feature detectors encoding information about visual and tactile cues, respectively (Fig. 7b).

The performance of the model neurons after learning matches well the Bayes-optimal MAP estimates that make use of knowledge about the exact relative noise variances. In contrast, averaging the two cues with equal weighting, and thus not exploiting the conductance-based opinion pooling, or considering only one of the two cues, would result in lower performance (Fig. 7c). Furthermore, the psychophysical curves of the trained model match well to experimental data obtained in a comparable setup (Fig. 7d,e).

Cross-modal suppression is caused by reliability-weighted opinions

Using the trained network from the previous section, we next consider the firing rate of the output neuron that prefers orientations $> 45^\circ$ for conflicting cues with a specific mismatch. We assume a stimulus orientation $> 45^\circ$ generates a separate cue for each modality, where, as an example we assume the visual cue to be more vertical than the tactile cue (Fig. 8a) which result in different dendritic reversal potentials E_i^d . In the following we identify the reliability of a stimulus with its intensity. Intuitively speaking, a weak stimulus is less reliable than a strong one.

When cues are presented simultaneously at low stimulus intensity, the output neurons fire stronger than in unimodal conditions (Fig. 8b). However, when presented simultaneously at high stimulus intensity the cues suppress each other, i.e., the resulting firing rate is less than the maximal rate in unimodal conditions

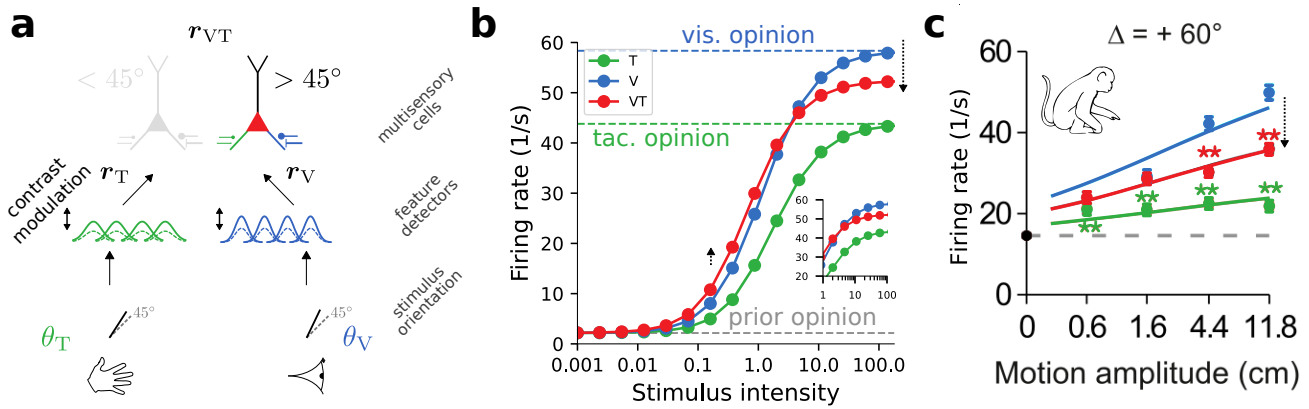


Figure 8: Cross-modal suppression as reliability-weighted opinion pooling. (a) Experimental setup (compare Fig. 7). (b) Firing rate of the output neuron encoding orientations $> 45^\circ$ for unimodal stimulation (V,T) and bimodal stimulation (VT). Dashed lines indicate the limit of no stimulation (gray), and infinitely strong tactile (green) and visual (blue) stimulation, respectively. Inset shows zoom in for high stimulation intensities. (c) Firing rate of a neuron from macaque MSTd in response to misaligned visual (blue) and vestibular (green) cues with a mismatch of $\Delta = 60^\circ$. Modified from [27]. Reprinted from *Neuron*, 95, Ohshiro, T., Angelaki, D. E. & DeAngelis, G. C., A neural signature of divisive normalization at the level of multisensory integration in primate cortex, 399–411, Copyright (2017), with permission from Elsevier.

(Fig. 8b). This phenomenon is known as cross-modal suppression [27, 28].

In the context of the opinion weighting, this counterintuitive interaction of multimodal cues arises as a consequence of the pooled opinion being a weighted average of the two unimodal opinions and the prior opinion. For low stimulus intensity the prior opinion dominates; since the evidence from either modality is only weak, the opinion arriving from a second modality always constitutes additional evidence that the preferred stimulus is present. Thus, the pooled opinion is pulled farther away from the prior in the bimodal condition as compared to the unimodal one. For high stimulus intensity the prior does not play a role and the pooled opinion becomes a weighted average of the two modality-specific opinions. As one cue is more aligned with the neuron’s preferred feature than the other, the weighted average appears as a suppression (Fig. 8). We thus propose that the computational principle of dendritic opinion pooling underlies other versions of cross-modal suppression [e.g., 6, 27–29], and also explains unimodal suppression arising from superimposing cues [e.g., 30–32], or superimposing sensory inputs and optogenetic stimulation [33, 34].

Discussion

The biophysics of cortical neurons can be interpreted in a Bayesian framework as reliability-weighted opinion pooling. In this framework, neurons encode posterior distributions via the mean and variance of their somatic membrane potential. We derived both membrane and weight dynamics from stochastic gradient ascent on a posterior distribution. Our plasticity rule naturally accommodates the relative reliabilities of different pathways by scaling up the relative weights of those inputs that have a high correlation to target potentials. The targets may themselves be formed by peri-somatic input from other modalities, or by more informed predictive input from other cortical areas. We demonstrated successful learning in a multisensory integration task in which modalities were different in their reliability. Without being explicitly constructed for this purpose, the trained model reproduces several experimental findings. Furthermore, it makes new experimental predictions, in particular regarding neuronal uncertainty representation and its learning. Our model adds support for the relevance of synaptic conductances

in shaping neuronal besides normalizing responses [6], and adapting the neuronal response time scale [35–38]. Previous work that stressed the sublinear voltage summation in conductance-based dendrites [17] is reinterpreted here from a functional perspective.

A common view of dendritic processing interprets the dendritic trees of neurons as two-layer networks, where non-linear responses are generated in dendritic branches and combined additively at the soma [39]. While such a view holds true for the distal tips, it can not hold for the entirety of the dendritic arborization [40]. Our current work thus provides a new paradigm that is particularly suited to synapses on proximal and intermediate dendritic branches (see also Supplement E, Fig 10). Furthermore, we have only considered synapses of which the conductance does not depend on the local membrane voltage. Excitatory synapses in pyramidal cells are known to express N-methyl-D-aspartate (NMDA) channels, whose conductance depends on the local voltage [41]. These synapses elicit strong supra-linear responses [42] which cause a massive increase of the isolated dendritic conductance and both dendritic and somatic potentials. In our present framework such responses correspond to an absolute certainty that a given feature is present in the input modality targeting the dendritic branch. Dendritic Ca-spikes, that originate in the apical dendrites of certain pyramidal cells [43, 44], could also correspond to such strong opinions. Our normative framework provides a mathematical underpinning for understanding such nonlinear effects. For example, synaptic conductances could be modeled to depend on the respective dendritic reversal potentials. While the principle of conductance-based opinion pooling applies independently of how conductances were generated, the dynamics of such a model would differ from the ones presented here.

Bayesian inference has previously been suggested as an operation on the level of a neuronal population in space [1, 16, 45] or in time [11, 46, 47]. In our framework, to read out the reliability of a single neuron’s opinion about the presence of its presynaptic feature, postsynaptic neurons either have to average across time or across a population of neurons that encode the same feature. Our single-neuron description of Bayesian inference is complementary to these population-based models. Other recent work also considers the neuronal representation and learning of uncertainty. In line with our plasticity rules, natural-gradient-descent learning for spiking neurons [48] predicts small learning rates for unreliable afferents. A different approach to representing and learning uncertainty is based on synaptic weights rather than membrane potentials and conductances [49]. In this model each synapse represents a distribution over synaptic weights and plasticity adapts the parameters of this distribution. While this represents an interesting complementary hypothesis, this normative view does not incorporate neuronal membrane dynamics.

In conclusion, we suggest that single cortical neurons are naturally equipped with the “cognitive capability” of Bayes-optimal opinion pooling. Moreover, our gradient-based formulation opens a promising avenue to explain the dynamics of hierarchically organized networks of such neurons. Our framework demonstrates that the conductance-based nature of synaptic coupling may not be an artifact of the biological substrate, but rather enables single neurons to perform efficient probabilistic inference previously thought to be realized only at the circuit level.

Methods

Equivalent somato-dendritic circuit

The excitatory and inhibitory dendritic conductances, g_i^E and g_i^I , are driven by the presynaptic firing rates $r(t)$ through synaptic weights $W_i^{E/I}$ and have the form $g_i^{E/I}(t) = W_i^{E/I} r(t)$. For notational simplicity we drop the time argument in the following. The dynamics of the somatic voltage u_s and dendritic voltages u_i^d

for the D dendrites projecting to the soma read as

$$C \dot{u}_s = g_0(E_0 - u_s) + \sum_{i=1}^D g_i^{\text{sd}}(u_i^{\text{d}} - u_s) \quad (6)$$

$$C_i^{\text{d}} \dot{u}_i^{\text{d}} = g_i^{\text{L}}(E^{\text{L}} - u_i^{\text{d}}) + g_i^{\text{E}}(E^{\text{E}} - u_i^{\text{d}}) + g_i^{\text{I}}(E^{\text{I}} - u_i^{\text{d}}) + g_i^{\text{ds}}(u_s - u_i^{\text{d}}), \quad (7)$$

where C and C_d are the somatic and dendritic capacitances, $E^{\text{L/E/I}}$ the reversal potentials for the leak, the excitatory and inhibitory currents, g_i^{sd} the transfer conductance from the i th dendrite to the soma, and g_i^{ds} in the reverse direction.

We assume that C^{d} s are small, so that dendritic dynamics are much faster than somatic dynamics and can thus be assumed to be in equilibrium. We can thus set \dot{u}_i^{d} to zero and rearrange Eqn. 7 to obtain

$$u_i^{\text{d}} - u_s = \frac{g_i^{\text{d}}}{g_i^{\text{d}} + g_i^{\text{ds}}}(E_i^{\text{d}} - u_s). \quad (8)$$

Plugging Eqn. 8 into Eqn. 6 and using the shorthand notation $\alpha_i^{\text{sd}} = \frac{g_i^{\text{sd}}}{g_i^{\text{ds}} + g_i^{\text{d}}}$, we obtain

$$C \dot{u}_s = g_0(E_0 - u_s) + \sum_{i=1}^D \alpha_i^{\text{sd}} g_i^{\text{d}}(E_i^{\text{d}} - u_s). \quad (9)$$

This is equivalent to gradient descent ($-\partial E/\partial u_s$) on the energy function

$$E(u_s) = \frac{g_0}{2}(E_0 - u_s)^2 + \sum_{i=1}^D \frac{\alpha_i^{\text{sd}} g_i^{\text{d}}}{2}(E_i^{\text{d}} - u_s)^2, \quad (10)$$

which also represents the log-posterior of the somatic potential distribution, as we discuss below.

Bayesian theory of somatic potential dynamics

Above, we have outlined a bottom-up derivation of somatic dynamics from the biophysics of structured neurons. In the following, we consider a probabilistic view of single neuron computation and demonstrate that this top-down approach yields exactly the same somatic membrane potential dynamics.

The assumption of Gaussian membrane potential densities throughout reflects the fact that the summation of many independent synaptic inputs generally yields a normal distribution, according to the central limit theorem and in agreement with experimental data [23]. We thus consider a prior distribution over u_s of the form

$$p(u_s|E_0, g_0) = \frac{1}{Z_0} e^{-\frac{g_0}{2\lambda_e}(E_0 - u_s)^2}, \quad (11)$$

with parameters λ_e, g_0, E_0 and normalization constant Z_0 . Similarly, we define the dendritic likelihood for u_s as

$$p(E_i^{\text{d}}|u_s, g_i^{\text{d}}) = \frac{1}{Z_i^{\text{d}}} e^{-\frac{\alpha_i^{\text{sd}} g_i^{\text{d}}}{2\lambda_e}(E_i^{\text{d}} - u_s)^2}, \quad (12)$$

with parameters $\alpha_i^{\text{sd}}, E_i^{\text{d}}, g_i^{\text{d}}$. According to Bayes' rule, the posterior distribution of the somatic membrane potential u_s is proportional to the product of the dendritic likelihoods and the prior. If we further assume

that dendrites are conditionally independent (conditional independence of dendritic likelihoods given the somatic potential), their joint likelihood $p(\mathbf{E}^d | u_s, \mathbf{g}^d)$ factorizes, yielding

$$p(u_s | E_0, g_0, \mathbf{E}^d, \mathbf{g}^d) \propto p(\mathbf{E}^d | u_s, \mathbf{g}^d) p(u_s | E_0, g_0) = \prod_{i=1}^D p(E_i^d | u_s, g_i^d) p(u_s | E_0, g_0). \quad (13)$$

Plugging in Eqs. 11 and 12, we can derive that the posterior is a Gaussian density over u_s with mean

$$\bar{E}_s = \frac{g_0 E_0 + \sum_{i=1}^D \alpha_i^{\text{sd}} g_i^d E_i^d}{g_0 + \sum_{i=1}^D \alpha_i^{\text{sd}} g_i^d} \quad (14)$$

and variance

$$\bar{g}_s = g_0 + \sum_{i=1}^D \alpha_i^{\text{sd}} g_i^d. \quad (15)$$

We thus obtain

$$p(u_s | W, r) \equiv p(u_s | E_0, g_0, \mathbf{E}^d, \mathbf{g}^d) = \frac{1}{Z} e^{-\frac{\bar{g}_s}{2\lambda_e} (u_s - \bar{E}_s)^2}, \quad (16)$$

with normalization factor $Z = \sqrt{\frac{2\pi\lambda_e}{\bar{g}_s}}$. We switched in Eqn. 16 to the conditioning on W and the presynaptic rates r since these uniquely determine the dendritic and somatic conductances (\mathbf{g}^d), and thus also the corresponding reversal potentials (\mathbf{E}^d). Here, we use the conventional linear relationship $g = Wr$ between conductances and presynaptic rates. For more complex synapses with nonlinear transmission of the type $g = f(w, r)$, where f can be an arbitrary function, our derivation holds similarly, but would yield a modified plasticity rule.

The energy function from Eqn. 10 is equivalent to $E(u_s) = -\lambda_e \log p(u_s | W, r) - \lambda_e \log Z = \frac{\bar{g}_s}{2} (u_s - \bar{E}_s)^2$. Since Z is independent of u_s , the somatic membrane potential dynamics from Eqn. 9 minimizes the energy E while maximizing the log-posterior,

$$C \dot{u}_s = -\frac{\partial E}{\partial u_s} = \lambda_e \frac{\partial}{\partial u_s} \log p(u_s | W, r). \quad (17)$$

In this form, the somatic voltage moves towards the maximum-a-posteriori estimate (MAP) of u_s . The stochastic version of Eqn. 17 with Gaussian additive noise leads to Eqn. 2 in the Results, effectively implementing Langevin sampling from the posterior distribution.

Weight dynamics

The KL between the target distribution p^* and the somatic membrane potential distribution can be written as

$$KL[p^*(u_s | r) | p(u_s | W, r)] = -S(p^*) - \mathbb{E}_{p^*} [\log p(u_s | W, r)]. \quad (18)$$

The entropy S of the target distribution p^* is independent of the synaptic weights W . Stochastic gradient descent on the KL divergence therefore leads to a learning rule for excitatory and inhibitory synapses that can be directly derived from Eqn. 16 (see SI):

$$\dot{W}_i^{\text{E/I}} \propto \lambda_e \frac{\partial}{\partial W_i^{\text{E/I}}} \log p(u_s^* | W, r) = \alpha_i^{\text{sd}} \left[(u_s^* - \bar{E}_s) (E^{\text{E/I}} - \tilde{E}_i^d) + \frac{\alpha_i^{\text{ds}}}{2} \left(\frac{\lambda_e}{\bar{g}_s} - (u_s^* - \bar{E}_s)^2 \right) \right] r, \quad (19)$$

with $\alpha_i^{\text{sd}} = \frac{g_i^{\text{sd}}}{g_i^{\text{ds}} + g_i^{\text{d}}}$, $\alpha_i^{\text{ds}} = \frac{g_i^{\text{ds}}}{g_i^{\text{ds}} + g_i^{\text{d}}}$ and $\tilde{E}_i^{\text{d}} = \alpha_i^{\text{ds}} \bar{E}_s + (1 - \alpha_i^{\text{ds}}) E_i^{\text{d}}$, see also Eqn. 5 in the Results, where we assumed symmetric coupling conductances between dendritic compartments and soma, i.e., $g_i^{\text{sd}} = g_i^{\text{ds}}$.

As discussed in the main text, the two terms in the plasticity rule roughly correspond to adapting the mean and variance of the somatic distribution. However, the second term $\propto \frac{\lambda_c}{g_s} - (u_s^* - \bar{E}_s)^2$ depends not only on a mismatch in the variance, but also on a mismatch in the mean of the distribution. To highlight this, we rewrite the sample u_s^* as the target mean plus a sample from $\mathcal{N}(0, 1)$ scaled with the target variance: $\frac{\lambda_c}{g_s} - (\mu^* + \sigma^* \xi^* - \bar{E}_s)^2$. In this form, one can easily see that only after \bar{E}_s matches the mean of the target distribution will the synapses adapt to match $\frac{\lambda_c}{g_s}$ to the target variance σ^{*2} .

In the absence of a target distribution, the neuron essentially sets its own targets. On average, weight changes in the absence of a target distribution are hence zero.

Since for conductance-based synapses only non-negative weights are meaningful, we define the minimal synaptic weight as zero.

Linear coordinates for nonlinear processing

The interplay of conductances and potentials can be visualized in a Cartesian plane spanned by inhibitory and excitatory conductances (Fig. 9). To simplify the picture, we neglect leak conductances and assume strong dendritic couplings $g^{\text{sd}}, g^{\text{ds}}$. The state of a single dendrite is fully determined by its inhibitory and excitatory synaptic conductances and can be represented by a vector $(g^{\text{I}}, g^{\text{E}})$. As we assume the prior conductance is zero, the total conductance at the soma is given by the sum of dendritic conductances. Thus, the soma itself can be represented by a vector that is the sum of the dendritic conductance vectors. Furthermore, the length of these vectors is proportional to the reliability of the opinion encoded by their associated compartments.

This simple, linear construction also allows us to determine the membrane potentials of individual compartments. For this, we need to construct the antidiagonal segment connecting the points $(1, 0)$ and $(0, 1)$. If one identifies the endpoints of this segment with the synaptic reversal potentials, i.e., $E^{\text{I}} \rightarrow (1, 0)$ and $E^{\text{E}} \rightarrow (0, 1)$, the antidiagonal can be viewed as a linear map of all possible membrane potentials. With this construction, the membrane potential of a compartment (dendritic or somatic) is simply given by the intersection of its conductance vector with the antidiagonal. Formally, this intersection is a nonlinear operation and instantiates a convex combination, the core computation that connects neuronal biophysics to Bayesian inference (Fig. 3).

This simple construction allows us to easily visualize the effects of synaptic weight changes on the dendritic and somatic opinions. For example, increasing the inhibitory conductance of a certain compartment will have a twofold effect: its opinion about the presence of its preferred feature will decrease (the intersection will move towards E^{I}), while simultaneously increasing its reliability (the vector will become longer).

In the following, we give a simple geometric proof that the intersection u of a conductance vector $(g^{\text{I}}, g^{\text{E}})$ with the antidiagonal indeed represents the correct membrane potential of the compartment. The coordinates of this intersection are easy to calculate as the solution to the system of equations that define the two lines $x/y = g^{\text{I}}/g^{\text{E}}$ and $y = 1 - x$, with

$$(x, y) = \left(\frac{g^{\text{I}}}{g^{\text{I}} + g^{\text{E}}}, \frac{g^{\text{E}}}{g^{\text{I}} + g^{\text{E}}} \right). \quad (20)$$

The ratio of these coordinates is also the ratio of the two resulting segments on the antidiagonal: $(E^{\text{E}} -$

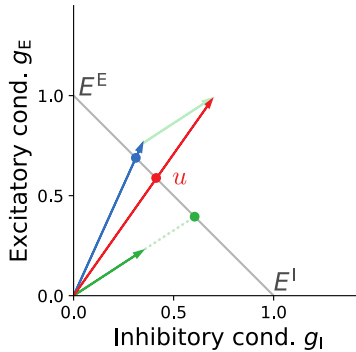


Figure 9: **The nonlinear membrane potential and synaptic dynamics expressed in linear conductance coordinates.** Dendrites can be represented as vectors defined by their inhibitory and excitatory conductances (blue and green arrows). In these coordinates, the soma is itself represented by a vector that is simply the sum of dendritic vectors (red arrow). The antidiagonal (gray) spans the range of all possible membrane voltages, from E^I to E^E . The membrane potential of any given compartment is given by the intersection of its conductance vector with the antidiagonal.

$u)/(u - E^I) = x/y$. Solving for u yields

$$u = \frac{g^I E^I + g^E E^E}{g^I + g^E}, \quad (21)$$

which represents the sought convex combination.

Simulation details

In the following we provide additional detail on simulations. Numerical values for all parameters can be found in the corresponding tables.

Details to Fig. 4 We consider the trained network from Fig. 7, but now use a finite somatic capacitance C . The differential equation of the output neurons (Eqn. 2) is integrated on a time grid of spacing Δt with an explicit Runge-Kutta method of order 3(2) from SciPy 1.4.1 [50]. To mimic background noise we generate “noise” cues, identical for both modalities, from a normal distribution $\mathcal{N}(\mu_b, \sigma_b^2)$ and convert these into rates r^b via the two populations of feature detectors. We consider an additional “signal” cue, also identical across modalities and trials, which generates additional rates r' via the feature detectors. The input rate for the output neurons is then computed as $r = \gamma r' + (1 - \gamma)r^b$, where $\gamma = \gamma^{\text{before}}$ before stimulus onset and $\gamma = \gamma^{\text{after}}$ after stimulus onset. For visualization purposes, we shift the scale of membrane potentials by -8mV in the figure.

Details to Fig. 6 We consider a neuron following instantaneous versions of Eqn. 2. It has D compartments with infinitely strong coupling of the dendritic compartments to the soma $g^{\text{ds}}, g^{\text{sd}} \rightarrow \infty$. In each trial, we sample a ground truth input rate $r \sim \mathcal{N}(\mu_r, \sigma_r^2)$, and from this rate we generate noisy rates $r^V \sim \mathcal{N}(r, \sigma_V^2), r^T \sim \mathcal{N}(r, \sigma_T^2)$ with modality-specific noise amplitudes σ_V, σ_T , respectively. We avoid non-positive input rates by replacing them with r_{\min} . We introduce an additional neuron with just a single compartments which generates target membrane potentials u^* from the ground truth input rate r and a random weight matrix. The second neuron receives the noisy input rates and should learn to mimic the distribution of somatic target potentials by learning synaptic weights via Eqn. 5. We train for a certain

Parameter name	Value	Description
N_{trials}	40	number of trials
$\mu^{\text{noise}}, \sigma^{\text{noise}}$	$35^\circ, 15^\circ$	mean/std. of noise orientations
θ_{stimulus}	44°	stimulus orientation
$\gamma^{\text{before}}, \gamma^{\text{after}}$	0.0, 0.88	rel. signal contrast before/after stimulus onset
dt	0.2 ms	integration time step
T	100 ms	simulation duration
C	50 pF	somatic membrane capacitance
λ_e	100.0 nS mV ²	neuronal exploration constant

Table 1: Parameters used in Fig. 4. Remaining parameters defined in Tab. 3.

Parameter name	Value	Description
N	1	number of neurons
D	2	number of dendritic compartments per neuron
g_0^L	0.25 nS	somatic leak conductance
g_i^L	0.025 nS	dendritic leak conductance
$w_{\text{init}}^{\text{min}}, w_{\text{init}}^{\text{max}}$	0.0 nS s, 0.019 nS s	min/max value of initial excitatory weights
$w_{\text{init}}^{\text{min}}, w_{\text{init}}^{\text{max}}$	0.0 nS s, 0.21 nS s	min/max value of initial inhibitory weights
$w_{\text{init}}^{\text{min}}, w_{\text{init}}^{\text{max}}$	0.0 nS s, 1.07 nS s	min/max value of target excitatory weights
$w_{\text{init}}^{\text{min}}, w_{\text{init}}^{\text{max}}$	0.0 nS s, 7.0 nS s	min/max value of target inhibitory weights
η	$1.25 \cdot 10^{-3}$	learning rate
N_{trials}	110000	number of trials
Δt_{trial}	10 ms	trial duration
r^*	$\mathcal{N}(1.2 \frac{1}{s}, 0.5 \frac{1}{s})$	distribution of input rates
r_{min}	$0.001 \frac{1}{s}$	minimal input rate
σ_T	$0.3 \frac{1}{s}$	noise amplitude of tactile modality
σ_V	$0.01875 \frac{1}{s}$	noise amplitude of visual modality

Table 2: Parameters used in Fig. 6. Remaining parameters defined in Tab. 3.

number of trials N_{trials} , and for visualization purposes convert trial number into time by defining a trial duration of Δt_{trial} .

Details to Fig. 7 We consider N output neurons each with D dendritic compartments. Their dynamics are described by Eqn.2, but for computational efficiency we consider an instantaneous version of with $C \rightarrow 0$. We furthermore assume infinitely strong coupling of the dendritic compartments to the soma $g^{\text{ds}}, g^{\text{sd}} \rightarrow \infty$. We use a softplus activation function $\rho(u_s) = \log(1 + \exp(u_s))$.

We define two homogeneous input populations of N_T and N_V feature detectors, respectively, with Gaussian tuning curves. The output rate of a feature detector in response to a cue with orientation θ is given by:

$$r(\theta) = r_{\text{min}} + (r_{\text{max}} - r_{\text{min}})e^{-\frac{\kappa}{2}(\theta - \theta')^2}, \quad (22)$$

with minimal rate r_{min} , maximal rate r_{max} , concentration κ and preferred orientation θ' . The preferred orientations θ' are homogeneously covering the interval $[\theta_{\text{min}}^{\text{fd}}, \theta_{\text{max}}^{\text{fd}}]$. All feature detectors from one population project to one dendritic compartment of each output neuron via plastic connections.

Each output neuron additionally receives an input from one presynaptic neuron with fixed rate but plastic weight, allowing it to adjust its prior opinions.

Initial weights are randomly sampled from a zero-mean normal distribution with standard deviation σ_{init}^w . Training proceeds as follows. From a ground-truth orientation θ^* two cues, θ_V , and θ_T , are generated by sampling from a Gaussian distribution around a true stimulus value with modality-specific noise amplitudes (σ_V and σ_T). The true orientation θ^* determines the output neurons target rates and hence, via the inverse activation function, target membrane potentials. The output neuron which should prefer orientations $> 45^\circ$ is trained to respond with a rate r_{low}^* if $\theta < 45^\circ$ and with a rate r_{high}^* if $\theta \geq 45^\circ$. The other output neuron is trained in the opposite fashion. Weight changes are following Eqn. 5. To speed up training we use batches of size b for N_{train} trials with ground truth orientations θ^* sampled uniformly from $[\theta_{\text{min}}^{\text{train}}, \theta_{\text{max}}^{\text{train}}]$. During training, with probability p_{bimodal} cues are provided via both modalities, while $1 - p_{\text{bimodal}}$ of all trials are unimodal, i.e., feature detectors of one modality remain silent.

For testing the output neurons are asked to classify N_{test} cues uniformly sampled from $[\theta_{\text{min}}^{\text{test}}, \theta_{\text{max}}^{\text{test}}]$, again perturbed by modality specific noise. The classification is performed on the combined rate of the two output neurons $r = 0.5 (r_0 + (r_{\text{low}} + r_{\text{high}} - r_1))$, where r_0 is the rate of the neuron preferring orientations $> 45^\circ$ and r_1 the rate of the other output neuron. A ground truth orientation θ^* is classified as $\geq 45^\circ$ if $r \geq r_{\text{low}} + 0.5 (r_{\text{high}} - r_{\text{low}})$.

Details to Fig. 8 We consider the trained network from Fig. 7. Here we set the cues provided to the feature detectors of the tactile and visual modality to fixed values θ_V, θ_T , respectively. We introduce two additional parameters, the stimulus intensities c_V, c_T , which linearly scale the rates of all feature detectors of the respective modality. For visualization purposes we scale the rate of the output neuron by a factor r_{scale} .

Acknowledgments

WS thanks M. Larkum and F. Helmchen for many inspiring discussions on dendritic processing, and M. Diamond and N. Nikbakht for sharing and discussing their data in an early state of this work. The authors thank all members of the CompNeuro and NeuroTMA groups for valuable discussions. This work has received funding from the European Union 7th Framework Programme under grant agreement 604102 (HBP), the Horizon 2020 Framework Programme under grant agreements 720270, 785907 and 945539 (HBP), the Swiss National Science Foundation (SNSF, Sinergia grant CRSII5-180316) and the Manfred Stärk Foundation.

Author contributions

JJ, JS, MAP, WS conceptualized the project; JJ, JS, WW, MAP, WS performed mathematical analyses; JJ, JS, WW performed computational modeling; JJ, MAP, WS wrote the original draft; JJ, WW, MAP, WS wrote the manuscript; all authors reviewed and edited the final manuscript; MAP, WS acquired funding; MAP, WS provided supervision.

Competing Interests Statement

The authors declare that they have no competing financial interests.

Parameter name	Value	Description
N	2	number of neurons
D	3	number of dendritic compartments per neuron
g_0^L	1.0 nS	somatic leak conductance
g_i^L	0.2 nS	dendritic leak conductance
E^E, E^I	0 mV, -85 mV	exc. /inh. reversal potentials
E^L	-70 mV	leak potential
λ_e	1.0 nS mV ²	neuronal exploration constant
C	$\rightarrow 0$	somatic membrane capacitance
g_i^{sd}, g_i^{ds}	$\rightarrow \infty$	somato-dendritic/dendro-somatic coupling conductance
N_T, N_V	70	number of feature detectors per modality
$[\theta_{\min}^{fd}, \theta_{\max}^{fd}]$	$[-315^\circ, 405^\circ]$	min/max preferred orientations of feature detectors
κ	$6.0 \frac{1}{\text{deg}^2}$	concentration (inverse variance) of feature detectors
$r_{\text{low}}, r_{\text{high}}$	$0.75 \frac{1}{s}, 16.0 \frac{1}{s}$	min/max rates of feature detectors
$w_{\text{init}}^{\min}, w_{\text{init}}^{\max}$	0.0 nS s, 0.005 nS s	min/max value of initial excitatory weights
$w_{\text{init}}^{\min}, w_{\text{init}}^{\max}$	0.0 nS s, 0.024 nS s	min/max value of initial inhibitory weights
η	$0.25 \cdot 10^{-4}$	learning rate
σ_T	28.5°	tactile noise amplitude
σ_V	13.5°	visual noise amplitude
$[\theta_{\min}^{\text{train}}, \theta_{\max}^{\text{train}}]$	$[-270^\circ, 360^\circ]$	min/max of training orientations
$[\theta_{\min}^{\text{test}}, \theta_{\max}^{\text{test}}]$	$[-135^\circ, 225^\circ]$	min/max of testing orientations
θ_{db}	45°	decision boundary
N_{train}	400 000	number of training trials
N_{test}	500 000	number of testing trials
p_{bimodal}	0.9	probability of a bimodal trial during training
b	12	batch size
$r_{\text{low}}^*, r_{\text{high}}^*$	$0.75 \frac{1}{s}, 16.0 \frac{1}{s}$	low/high target rates

Table 3: Parameters used in Fig. 7.

Parameter name	Value	Description
θ_T	65°	orientation of tactile cue
θ_V	50°	orientation of visual cue
c_T, c_V	$[10^{-3}, 10^2]$	stimulus contrasts of tactile and visual modality
r_{scale}	2.5	output rate scaling factor

Table 4: Parameters used in Fig. 8. Remaining parameters defined in Tab. 3.

References

1. Ma, W. J., Beck, J. M., Latham, P. E. & Pouget, A. Bayesian inference with probabilistic population codes. *Nature neuroscience* **9**, 1432 (2006).
2. Echeveste, R., Aitchison, L., Hennequin, G. & Lengyel, M. Cortical-like dynamics in recurrent circuits optimized for sampling-based probabilistic inference. *Nature Neuroscience* **23**, 1138–1149 (2020).
3. Ernst, M. O. & Banks, M. S. Humans integrate visual and haptic information in a statistically optimal fashion. *Nature* **415**, 429 (2002).
4. Knill, D. C. & Saunders, J. A. Do humans optimally integrate stereo and texture information for judgments of surface slant? *Vision research* **43**, 2539–2558 (2003).
5. Hillis, J. M., Watt, S. J., Landy, M. S. & Banks, M. S. Slant from texture and disparity cues: Optimal cue combination. *Journal of vision* **4**, 1–1 (2004).
6. Carandini, M. & Heeger, D. J. Summation and division by neurons in primate visual cortex. *Science* **264**, 1333–1336 (1994).
7. Urbanczik, R. & Senn, W. Learning by the dendritic prediction of somatic spiking. *Neuron* **81**, 521–528 (2014).
8. Rock, I. & Victor, J. Vision and touch: An experimentally created conflict between the two senses. *Science* **143**, 594–596 (1964).
9. Alais, D. & Burr, D. The ventriloquist effect results from near-optimal bimodal integration. *Current biology* **14**, 257–262 (2004).
10. Fetsch, C. R., Turner, A. H., DeAngelis, G. C. & Angelaki, D. E. Dynamic reweighting of visual and vestibular cues during self-motion perception. *Journal of Neuroscience* **29**, 15601–15612 (2009).
11. Fischer, B. J. & Peña, J. L. Owl’s behavior and neural representation predicted by Bayesian inference. *Nature neuroscience* **14**, 1061 (2011).
12. Raposo, D., Sheppard, J. P., Schrater, P. R. & Churchland, A. K. Multisensory decision-making in rats and humans. *Journal of Neuroscience* **32**, 3726–3735 (2012).
13. Nikbakht, N., Tafreshiha, A., Zoccolan, D. & Diamond, M. E. Supralinear and supramodal integration of visual and tactile signals in rats: psychophysics and neuronal mechanisms. *Neuron* **97**, 626–639 (2018).
14. Xu, Y., Regier, T. & Newcombe, N. S. An adaptive cue combination model of human spatial reorientation. *Cognition* **163**, 56–66 (2017).
15. Darlington, T. R., Beck, J. M. & Lisberger, S. G. Neural implementation of Bayesian inference in a sensorimotor behavior. *Nature neuroscience* **21**, 1442 (2018).
16. Knill, D. C. & Pouget, A. The Bayesian brain: the role of uncertainty in neural coding and computation. *TRENDS in Neurosciences* **27**, 712–719 (2004).
17. Tran-Van-Minh, A. *et al.* Contribution of sublinear and supralinear dendritic integration to neuronal computations. *Frontiers in cellular neuroscience* **9**, 67 (2015).
18. Crochet, S., Poulet, J. F., Kremer, Y. & Petersen, C. C. Synaptic mechanisms underlying sparse coding of active touch. *Neuron* **69**, 1160–1175 (2011).

19. Monier, C., Chavane, F., Baudot, P., Graham, L. J. & Frégnac, Y. Orientation and direction selectivity of synaptic inputs in visual cortical neurons: a diversity of combinations produces spike tuning. *Neuron* **37**, 663–680 (2003).
20. Churchland, M. M. *et al.* Stimulus onset quenches neural variability: a widespread cortical phenomenon. *Nature neuroscience* **13**, 369 (2010).
21. Sachidhanandam, S., Sreenivasan, V., Kyriakatos, A., Kremer, Y. & Petersen, C. C. Membrane potential correlates of sensory perception in mouse barrel cortex. *Nat. Neurosci.* **16**, 1671–1677 (2013).
22. Hénaff, O. J., Boundy-Singer, Z. M., Meding, K., Ziemba, C. M. & Goris, R. L. Representation of visual uncertainty through neural gain variability. *Nature communications* **11**, 1–12 (2020).
23. Petersen, P. C. & Berg, R. W. Lognormal firing rate distribution reveals prominent fluctuation-driven regime in spinal motor networks. *eLife* **5**, 1–33. ISSN: 2050084X (2016).
24. Richardson, M. J. & Gerstner, W. Synaptic shot noise and conductance fluctuations affect the membrane voltage with equal significance. *Neural computation* **17**, 923–947 (2005).
25. Jordan, J. *et al.* Deterministic networks for probabilistic computing. *Scientific reports* **9**, 1–17 (2019).
26. Urbanczik, R. & Senn, W. Learning by the Dendritic Prediction of Somatic Spiking. *Neuron* **81**, 521–528 (2014).
27. Ohshiro, T., Angelaki, D. E. & DeAngelis, G. C. A neural signature of divisive normalization at the level of multisensory integration in primate cortex. *Neuron* **95**, 399–411 (2017).
28. Fetsch, C. R., DeAngelis, G. C. & Angelaki, D. E. Bridging the gap between theories of sensory cue integration and the physiology of multisensory neurons. *Nature Reviews Neuroscience* **14**, 429 (2013).
29. Meijer, G. T., Montijn, J. S., Pennartz, C. M. & Lansink, C. S. Audiovisual modulation in mouse primary visual cortex depends on cross-modal stimulus configuration and congruency. *Journal of Neuroscience* **37**, 8783–8796 (2017).
30. Morrone, M. C., Burr, D. & Maffei, L. Functional implications of cross-orientation inhibition of cortical visual cells. I. Neurophysiological evidence. *Proceedings of the Royal Society of London. Series B. Biological Sciences* **216**, 335–354 (1982).
31. Carandini, M., Heeger, D. J. & Movshon, J. A. Linearity and normalization in simple cells of the macaque primary visual cortex. *Journal of Neuroscience* **17**, 8621–8644 (1997).
32. Busse, L., Wade, A. R. & Carandini, M. Representation of concurrent stimuli by population activity in visual cortex. *Neuron* **64**, 931–942 (2009).
33. Sato, T. K., Häusser, M. & Carandini, M. Distal connectivity causes summation and division across mouse visual cortex. *Nature neuroscience* **17**, 30 (2014).
34. Nassi, J. J., Avery, M. C., Cetin, A. H., Roe, A. W. & Reynolds, J. H. Optogenetic activation of normalization in alert macaque visual cortex. *Neuron* **86**, 1504–1517 (2015).
35. Destexhe, A., Rudolph, M. & Paré, D. The high-conductance state of neocortical neurons in vivo. *Nature Reviews Neuroscience* **4**, 739–751 (2003).
36. Güttig, R. & Sompolinsky, H. Time-warp-invariant neuronal processing. *PLoS Biol* **7**, e1000141 (2009).
37. Silver, R. A. Neuronal arithmetic. *Nature Reviews Neuroscience* **11**, 474–489 (2010).

38. Petrovici, M. A., Bill, J., Bytschok, I., Schemmel, J. & Meier, K. Stochastic inference with spiking neurons in the high-conductance state. *Physical Review E* **94**, 042312 (2016).
39. Poirazi, P., Brannon, T. & Mel, B. W. Pyramidal neuron as two-layer neural network. *Neuron* **37**, 989–999 (2003).
40. Wybo, W. A., Torben-Nielsen, B., Nevian, T. & Gewaltig, M. O. Electrical Compartmentalization in Neurons. *Cell Reports* **26**, 1759–1773.e7. ISSN: 22111247. <https://doi.org/10.1016/j.celrep.2019.01.074> (2019).
41. MacDonald, J. F. & Wojtowicz, J. M. The effects of L-glutamate and its analogues upon the membrane conductance of central murine neurones in culture. *Canadian Journal of Physiology and Pharmacology* **60**, 282–296. eprint: <https://doi.org/10.1139/y82-039>. <https://doi.org/10.1139/y82-039> (1982).
42. Schiller, J., Major, G., Koester, H. & Schiller, Y. NMDA spikes in basal dendrites of cortical pyramidal neurons. *Nature* **1261**, 285–289. <http://www.nature.com/nature/journal/v404/n6775/abs/404285a0.html> (2000).
43. Larkum, M. E., Zhu, J. J. & Sakmann, B. A new cellular mechanism for coupling inputs arriving at different cortical layers. *Nature* **398**, 338–41. ISSN: 0028-0836. <http://www.ncbi.nlm.nih.gov/pubmed/10192334> (Mar. 1999).
44. London, M. & Häusser, M. Dendritic Computation. *Annual Review of Neuroscience* **28**, 503–532 (2005).
45. Körding, K. P., Ko, K. P. & Wolpert, D. M. Bayesian decision theory in sensorimotor control. *Trends in cognitive sciences* **10**, 319–26 (2006).
46. Orbán, G., Berkes, P., Fiser, J. & Lengyel, M. Neural variability and sampling-based probabilistic representations in the visual cortex. *Neuron* **92**, 530–543 (2016).
47. Dold, D. *et al.* Stochasticity from function—why the bayesian brain may need no noise. *Neural networks* **119**, 200–213 (2019).
48. Kreutzer, E., Petrovici, M. A. & Senn, W. *Natural gradient learning for spiking neurons in Proceedings of the Neuro-inspired Computational Elements Workshop* (2020), 1–3.
49. Aitchison, L. *et al.* Synaptic plasticity as Bayesian inference. *Nature Neuroscience*, 1–7 (2021).
50. Virtanen, P. *et al.* SciPy 1.0: fundamental algorithms for scientific computing in Python. *Nature methods* **17**, 261–272 (2020).
51. Wybo, W. A. *et al.* Data-driven reduction of dendritic morphologies with preserved dendro-somatic responses. *eLife* **10**, 1–26 (2021).
52. Hay, E., Hill, S., Schürmann, F., Markram, H. & Segev, I. Models of neocortical layer 5b pyramidal cells capturing a wide range of dendritic and perisomatic active properties. *PLoS computational biology* **7**, e1002107 (July 2011).

Supplements

A Definitions

The following definitions are used throughout the supplementary material and main manuscript:

$$\begin{aligned}
 u_s &= \text{somatic membrane potential} \\
 \lambda_e &= \text{neuronal exploration parameter} \\
 W_i^{E/I} &= \text{excitatory/inhibitory synaptic weights onto dendrite } i \\
 r &= \text{presynaptic rates} \\
 g_i^L &= \text{leak conductance on dendrite } i \\
 g_i^{E/I} &= W_i^{E/I} r, \text{ excitatory/inhibitory conductance on dendrite } i \\
 E^{L/E/I} &= \text{leak/excitatory/inhibitory reversal potential} \\
 g_0 &= \text{prior conductance} \\
 E_0 &= \text{prior potential} \\
 g_i^d &= g_i^E + g_i^I + g_i^L \text{ isolated dendritic conductance} \\
 E_i^d &= \frac{g_i^E E^E + g_i^I E^I + g_i^L E^L}{g_i^E + g_i^I + g_i^L} \text{ dendritic reversal potential} \\
 g_i^{sd} &= \text{dendro-somatic coupling conductance} \\
 g_i^{ds} &= \text{somato-dendritic coupling conductance} \\
 \alpha_i^{sd} &= \frac{g_i^{sd}}{g_i^{ds} + g_i^d} \text{ dendro-somatic coupling factor} \\
 \alpha_i^{ds} &= \frac{g_i^{ds}}{g_i^{ds} + g_i^d} \text{ somato-dendritic coupling factor} \\
 \bar{g}_s &= g_0 + \sum_{i=1}^D \alpha_i^{sd} g_i^d \text{ total somatic condutance} \\
 \bar{E}_s &= \frac{1}{\bar{g}_s} \left(g_0 E_0 + \sum_{i=1}^D \alpha_i^{sd} g_i^d E_i^d \right) \text{ pooled somatic opinion}
 \end{aligned}$$

B Derivation of the somatic potential distribution

We consider the prior distribution on u_s of the form

$$p(u_s | E_0, g_0) = \frac{1}{Z_0} e^{-\frac{g_0}{2\lambda_e} (E_0 - u_s)^2}. \quad (23)$$

We consider the dendritic likelihood functions for u_s :

$$p(E_i^d | u_s, g_i^d) = \frac{1}{Z_i^d} e^{-\frac{\alpha_i^{sd} g_i^d}{2\lambda_e} (E_i^d - u_s)^2}. \quad (24)$$

The posterior over u_s is given by

$$p(u_s | E_0, g_0, \mathbf{E}^d, \mathbf{g}^d) \propto p(\mathbf{E}^d | u_s, \mathbf{g}^d) p(u_s | E_0, g_0) = \prod_{i=1}^D p(E_i^d | u_s, g_i^d) p(u_s | E_0, g_0). \quad (25)$$

We first consider the unnormalized posterior, and rewrite it, dropping all terms constant in u_s :

$$\begin{aligned} \prod_{i=1}^D p(E_i^d | u_s, g_i^d) p(u_s | E_0, g_0) &\propto e^{-\frac{g_0}{2\lambda_e}(u_s - E_0)^2} \prod_{i=1}^D e^{-\frac{\alpha_i^{\text{sd}} g_i^d}{2\lambda_e}(u_s - E_i^d)^2} \\ &\propto e^{-\frac{g_0 + \sum_{i=1}^D \alpha_i^{\text{sd}} g_i^d}{2\lambda_e} \left(u_s^2 - 2u_s \frac{g_0 E_0 + \sum_{i=1}^D \alpha_i^{\text{sd}} g_i^d E_i^d}{g_0 + \sum_{i=1}^D \alpha_i^{\text{sd}} g_i^d} \right)} \end{aligned} \quad (26)$$

$$\propto e^{-\frac{\bar{g}_s}{2\lambda_e}(u_s - \bar{E}_s)^2} \quad (27)$$

As the density needs to be normalized, we can compute the normalization factor Z directly from this form as a Gaussian integral:

$$\begin{aligned} Z &= \int du_s e^{-\frac{\bar{g}_s}{2\lambda_e}(u_s - \bar{E}_s)^2} \\ &= \sqrt{\frac{2\pi\lambda_e}{\bar{g}_s}} \end{aligned} \quad (28)$$

This finally results in the somatic potential distribution:

$$p(u_s | W, r) = \frac{1}{Z} e^{-\frac{\bar{g}_s}{2\lambda_e}(u_s - \bar{E}_s)^2}. \quad (29)$$

C Derivation of membrane potential dynamics

We introduce the energy E as the negative logarithm of p :

$$E(u_s, W, r) := -\log p(u_s | W, r). \quad (30)$$

We obtain potential dynamics from gradient descent on E :

$$\begin{aligned} c_m \dot{u}_s &= -\lambda_e \frac{\partial}{\partial u_s} E(u_s, W, r) \\ &= \lambda_e \frac{\partial}{\partial u_s} \log p(u_s | W, r) \\ &= \lambda_e \frac{\partial}{\partial u_s} \left(-\frac{\bar{g}_s}{2\lambda_e} (u_s - \bar{E}_s)^2 + \frac{1}{2} \log \frac{\bar{g}_s}{2\pi\lambda_e} \right) \\ &= \bar{g}_s (\bar{E}_s - u_s) \\ &= g_0 (E_0 - u_s) + \sum_{i=1}^D \alpha_i^{\text{sd}} (g_i^L (E^L - u_s) + g_i^E (E^E - u_s) + g_i^I (E^I - u_s)). \end{aligned} \quad (31)$$

D Derivation of weight dynamics

We want to obtain weight dynamics that approximate gradient descent on the KL:

$$-\lambda_e \frac{\partial}{\partial W_i^{E/I}} \mathbb{E}_r [\text{KL}(p^*(u_s|r) \| p(u_s|W, r))] \quad (32)$$

We first rewrite the KL:

$$\begin{aligned} \text{KL}(p^*(u_s|r) \| p(u_s|W, r)) &= \int du_s p^*(u_s|r) \log \frac{p^*(u_s|r)}{p(u_s|W, r)} \\ &= \int du_s p^*(u_s|r) \log p^*(u_s|r) - \int du_s p^*(u_s|r) \log p(u_s|W, r) \\ &= -S(p^*(u_s|r)) - \mathbb{E}_{u_s} [\log p(u_s|W, r)] \end{aligned}$$

Here, we can drop the first term as it does not depend on W . We perform stochastic gradient descent in r and u_s , i.e., we drop the averages and use single samples $r \sim p^*(r), u^* \sim p^*(u_s|r)$:

$$\begin{aligned} \lambda_e \frac{\partial}{\partial W_i^{E/I}} \mathbb{E}_r [\mathbb{E}_{u_s} [\log p(u_s|W, r)]] &= \lambda_e \frac{\partial}{\partial W_i^{E/I}} \int dr p^*(r) \int du_s p^*(u_s|r) \log p(u_s|W, r) \\ &\approx \lambda_e \frac{\partial}{\partial W_i^{E/I}} \log p(u^*|W, r), \end{aligned} \quad (33)$$

where in the last step we plugged in the empirical distribution for $p^*(r)p^*(u_s|r)$ consisting of Dirac-delta functions centered on the data points (r, u^*) . We set

$$\dot{W}_i^{E/I} = \eta \lambda_e \frac{\partial}{\partial W_i^{E/I}} \log p(u^*|W, r) \quad (34)$$

with some fixed learning rate η .

We compute the derivative:

$$\begin{aligned} \lambda_e \frac{\partial}{\partial W_i^{E/I}} \log p(u_s|W, r) &= \lambda_e \frac{\partial}{\partial W_i^{E/I}} \left(-\frac{\bar{g}_s}{2\lambda_e} (u_s - \bar{E}_s)^2 + \frac{1}{2} \log \frac{\bar{g}_s}{2\pi\lambda_e} \right) \\ &= -\frac{1}{2} \frac{\partial \bar{g}_s}{\partial W_i^{E/I}} (u_s - \bar{E}_s)^2 - \frac{\bar{g}_s}{2} \frac{\partial}{\partial W_i^{E/I}} (u_s - \bar{E}_s)^2 + \frac{\lambda_e}{2} \frac{\partial}{\partial W_i^{E/I}} \log \bar{g}_s \end{aligned} \quad (35)$$

We compute the derivative:

$$\begin{aligned} \frac{\partial \bar{g}_s}{\partial W_i^{E/I}} &= \frac{\partial}{\partial W_i^{E/I}} \left(g_0 + \sum_{d=1}^D \frac{g_i^{\text{sd}}}{g_i^{\text{ds}} + g_i^{\text{d}}} g_i^{\text{d}} \right) \\ &= \frac{\partial}{\partial W_i^{E/I}} \frac{g_i^{\text{sd}}}{g_i^{\text{ds}} + g_i^{\text{d}}} g_i^{\text{d}} \\ &= \left(\frac{\partial}{\partial W_i^{E/I}} \frac{g_i^{\text{sd}}}{g_i^{\text{ds}} + g_i^{\text{d}}} \right) g_i^{\text{d}} + \frac{g_i^{\text{sd}}}{g_i^{\text{ds}} + g_i^{\text{d}}} \frac{\partial}{\partial W_i^{E/I}} g_i^{\text{d}} \\ &= \left(-\frac{g_i^{\text{sd}}}{(g_i^{\text{ds}} + g_i^{\text{d}})^2} \frac{\partial}{\partial W_i^{E/I}} g_i^{\text{d}} \right) g_i^{\text{d}} + \frac{g_i^{\text{sd}}}{g_i^{\text{ds}} + g_i^{\text{d}}} \frac{\partial}{\partial W_i^{E/I}} g_i^{\text{d}} \\ &= \left[\left(-\frac{g_i^{\text{sd}}}{(g_i^{\text{ds}} + g_i^{\text{d}})^2} \right) g_i^{\text{d}} + \frac{g_i^{\text{sd}}}{g_i^{\text{ds}} + g_i^{\text{d}}} \right] r \\ &= \alpha_i^{\text{sd}} \alpha_i^{\text{ds}} r \end{aligned} \quad (36)$$

with $\alpha_i^{\text{sd}} := \frac{g_i^{\text{sd}}}{g_i^{\text{ds}} + g_i^{\text{d}}}$ and $\alpha_i^{\text{ds}} := \frac{g_i^{\text{ds}}}{g_i^{\text{ds}} + g_i^{\text{d}}}$. Note that for symmetric coupling conductances $\alpha_i^{\text{sd}} = \alpha_i^{\text{ds}}$.

We compute the derivative:

$$\begin{aligned}
\frac{\partial}{\partial W_i^{\text{E/I}}} (u_s - \bar{E}_s)^2 &= -2(u_s - \bar{E}_s) \frac{\partial}{\partial W_i^{\text{E/I}}} \bar{E}_s \\
&= -2(u_s - \bar{E}_s) \frac{\partial}{\partial W_i^{\text{E/I}}} \left[\frac{1}{\bar{g}_s} \left(g_0 E_0 + \sum_{d=1}^D \frac{g_i^{\text{sd}}}{g_i^{\text{ds}} + g_i^{\text{d}}} g_i^{\text{d}} E_i^{\text{d}} \right) \right] \\
&= -2(u_s - \bar{E}_s) \left(-\frac{1}{\bar{g}_s} \bar{E}_s \frac{\partial \bar{g}_s}{\partial W_i^{\text{E/I}}} + \frac{1}{g_0} \frac{\partial}{\partial W_i^{\text{E/I}}} \left[\frac{g_i^{\text{sd}}}{g_i^{\text{ds}} + g_i^{\text{d}}} g_i^{\text{d}} E_i^{\text{d}} \right] \right) \\
&= -2(u_s - \bar{E}_s) \left(-\frac{1}{\bar{g}_s} \bar{E}_s \frac{\partial \bar{g}_s}{\partial W_i^{\text{E/I}}} + \frac{1}{\bar{g}_s} \left[\frac{\partial}{\partial W_i^{\text{E/I}}} \frac{g_i^{\text{sd}}}{g_i^{\text{ds}} + g_i^{\text{d}}} \right] g_i^{\text{d}} E_i^{\text{d}} + \frac{1}{\bar{g}_s} \left[\frac{g_i^{\text{sd}}}{g_i^{\text{ds}} + g_i^{\text{d}}} \right] E^{\text{E/I}} r \right) \\
&= -2(u_s - \bar{E}_s) \left(-\frac{1}{\bar{g}_s} \bar{E}_s \alpha_i^{\text{sd}} \alpha_i^{\text{ds}} r - \frac{\alpha_i^{\text{sd}}}{\bar{g}_s} \left[\frac{1}{g_i^{\text{ds}} + g_i^{\text{d}}} r \right] g_i^{\text{d}} E_i^{\text{d}} + \frac{\alpha_i^{\text{sd}}}{\bar{g}_s} E^{\text{E/I}} r \right) \\
&= -2(u_s - \bar{E}_s) \frac{\alpha_i^{\text{sd}}}{\bar{g}_s} \left(-\bar{E}_s \alpha_i^{\text{ds}} - \left[\frac{g_i^{\text{d}}}{g_i^{\text{ds}} + g_i^{\text{d}}} \right] E_i^{\text{d}} + E^{\text{E/I}} \right) r \\
&= -2(u_s - \bar{E}_s) \frac{\alpha_i^{\text{sd}}}{\bar{g}_s} \left(E^{\text{E/I}} - \left[\alpha_i^{\text{ds}} \bar{E}_s + (1 - \alpha_i^{\text{ds}}) E_i^{\text{d}} \right] \right) r
\end{aligned} \tag{37}$$

We compute the derivative:

$$\begin{aligned}
\frac{\partial}{\partial W_i^{\text{E/I}}} \log \bar{g}_s &= \frac{1}{\bar{g}_s} \frac{\partial \bar{g}_s}{\partial W_i^{\text{E/I}}} \\
&= \frac{1}{\bar{g}_s} \alpha_i^{\text{sd}} \alpha_i^{\text{ds}} r
\end{aligned} \tag{38}$$

We now put everything together, yielding:

$$\begin{aligned}
\lambda_e \frac{\partial}{\partial W_i^{\text{E/I}}} \log p(u^* | W, r) &= -\frac{1}{2} \frac{\partial \bar{g}_s}{\partial W_i^{\text{E/I}}} (u^* - \bar{E}_s)^2 - \frac{\bar{g}_s}{2} \frac{\partial}{\partial W_i^{\text{E/I}}} (u^* - \bar{E}_s)^2 + \frac{\lambda_e}{2} \frac{\partial}{\partial W_i^{\text{E/I}}} \log \bar{g}_s \\
&= -\frac{1}{2} \alpha_i^{\text{sd}} \alpha_i^{\text{ds}} r (u^* - \bar{E}_s)^2 + (u^* - \bar{E}_s) \alpha_i^{\text{sd}} \left(E^{\text{E/I}} - \left[\alpha_i^{\text{ds}} \bar{E}_s + (1 - \alpha_i^{\text{ds}}) E_i^{\text{d}} \right] \right) r + \frac{1}{2} \frac{\lambda_e}{\bar{g}_s} \alpha_i^{\text{sd}} \alpha_i^{\text{ds}} r \\
&= \left[(u^* - \bar{E}_s) \left(E^{\text{E/I}} - \left[\alpha_i^{\text{ds}} \bar{E}_s + (1 - \alpha_i^{\text{ds}}) E_i^{\text{d}} \right] \right) - \frac{\alpha_i^{\text{ds}}}{2} \left((u^* - \bar{E}_s)^2 - \frac{\lambda_e}{\bar{g}_s} \right) \right] \alpha_i^{\text{sd}} r \\
&= \left[(u^* - \bar{E}_s) \left(E^{\text{E/I}} - \tilde{E}_i^{\text{d}} \right) - \frac{\alpha_i^{\text{ds}}}{2} \left((u^* - \bar{E}_s)^2 - \frac{\lambda_e}{\bar{g}_s} \right) \right] \alpha_i^{\text{sd}} r
\end{aligned} \tag{39}$$

where we introduced $\tilde{E}_i^{\text{d}} = \alpha_i^{\text{ds}} \bar{E}_s + (1 - \alpha_i^{\text{ds}}) E_i^{\text{d}}$.

E Dendritic parameters

Our approach relies on two assumptions with respect to the biophysical model (Eqs. 6, 7): the capacitances of the dendritic compartments are small compared to the somatic capacitance and the dendritic conductances g_i^{d} are able to overrule the somatic prior g_0 . A recently developed dendritic simplification

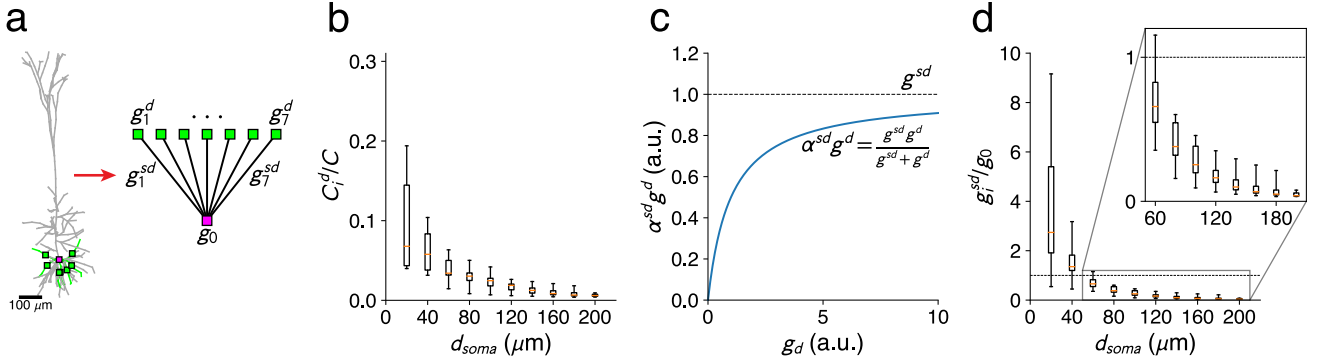


Figure 10: **Parameters of the reduced compartmental model as derived from a detailed morphological model.** (a) A detailed L5 Pyramidal cell model (left) is reduced to a configuration with one dendritic compartment on each of seven main basal subtrees (right). (b) Ratio of dendritic to somatic capacitance, for increasing distances between the dendritic sites and the soma. The box indicates the lower and upper quartile values and the orange bar the median. The whiskers indicate the minimal and maximal values. The ratio is always much smaller than one, supporting our approximation of using the instantaneous solution for the dendritic voltage. (c) Effective dendritic conductance at the soma, $\alpha_i^{sd} g_i^d$, as a function of the isolated dendritic conductance g_i^d . This quantity represents the effective reliability of the dendritic opinion as read out at the soma. It saturates at the level of the somato-dendritic coupling conductance g_i^{sd} . (d) Ratio of the somato-dendritic coupling conductance to the somatic leak conductance for increasing distance between the dendritic site and the soma. When this ratio is larger than one, a single branch can overrule the somatic prior. Otherwise, multiple branches have to cooperate to overrule the prior. The inset shows a magnified version for dendritic sites farther than 50 μm from the soma.

framework [51] allows us to systematically reduce full biophysical models to obtain the parameters of the reduced compartmental models (Eqs. 6, 7) used in this work. Given a set of dendritic locations on the morphology along the dendritic tree, this approach yields capacitances, leak conductances and coupling conductances for the simplified model that optimally reproduce the dynamics of the full model, at those chosen locations (Fig. 10a). This, in turns, allows us to assert the validity of the aforementioned assumptions.

We use a detailed biophysical model of an L5 pyramidal cell [52]. Without synaptic input, the ion channels in this model collectively determine the cell's prior, encoded in the resting membrane potential and the total conductance at rest. Per dendritic segment, we aggregate these conductance contributions into a single, prior conductance. Formally, this conductance is a passive leak, and the resulting model is a passive model with the same prior (and morphology) as the detailed model.

Then, we choose dendritic sites that allow us to test the validity of our assumptions. The morphology has seven basal dendritic subtrees with branches of at least 200 μm . In each subtree, we select one such branch (green in Fig. 10a), and place a single dendritic location on each of those branches at a given distance from the soma. We increase the distance between soma and dendritic sites in increments of 20 μm and derive a reduced compartmental model for each configuration (Fig. 10a). We then compare the ratios of dendritic capacitance C_i^d and somatic capacitance C for the seven compartments $i \in \{1, \dots, 7\}$. We find that these ratio are much smaller than one, no matter the distance from the soma (Fig. 10b).

Then, we asses the theoretical maximum degree to which synapses placed at the dendritic sites under investigation can contribute to overruling the somatic prior. The effective dendritic conductance of compartment i , measured at the soma, is given by $\alpha_i^{sd} g_i^d$ (Eqn. 9). This function has an asymptotic maximum at the dendro-somatic coupling conductance g_i^{sd} (Fig. 10c). In consequence, g_i^{sd} is the theoretical maximal conductance that dendritic synapses in compartment i can exert at the soma. We thus need to

compare g_i^{sd} with the somatic prior g_0 (Fig. 10d). For a distance between soma and dendritic site smaller than $\sim 50\mu\text{m}$, we find that a single branch can overrule the prior, as the ratio g_i^{sd}/g_0 is typically larger than one. For larger distances, multiple branches have to collaborate to overrule the prior (Fig. 10D, inset).